AIAA 81-0051R

Viscous-Inviscid Interaction on Oscillating Airfoils in Subsonic Flow

W. J. McCroskey* and S. L. Pucci†
U.S. Army Aeromechanics Laboratory (AVRADCOM)
Ames Research Center, Moffett Field, Calif.

Selected results from an extensive oscillating airfoil experiment are analyzed and reviewed. Four distinct regimes of viscous-inviscid interaction are identified, corresponding to varying degrees of unsteady flow separation. The dominant fluid dynamic phenomena are described for each regime. Ten specific test cases, including the appropriate flow conditions and experimental results, are proposed for evaluating unsteady viscous theories and computational methods.

I. Introduction

IMPORTANT viscous phenomena combine with unsteady effects in a variety of current aeronautical, hydrodynamic, and wind-energy problems. Consequently, several recent investigations have attempted to predict, compute, or empirically correlate the unsteady airloads on oscillating airfoils that experience varying degrees of flow separation, and additional work is in progress at a number of research centers. The results are mixed, and conflicting claims abound; partly because the difficulty of the problem increases rapidly with increasing amounts of separation and partly because definitive data over wide ranges of separated flow conditions do not exist.

The authors and their colleagues have recently concluded an extensive experimental investigation of boundary-layer transition, separation, and unsteady stall on oscillating airfoils in two-dimensional subsonic flow. The experiment included more than 50 combinations of M_∞ and parameters of the unsteady motion for each of eight different airfoil sections. Highlights of some of the extensive lift, drag, and pitching moment data were described recently in Ref. 1. The purpose of the present paper is to extract, from a limited number of the aggregate of test points, the specific details and experimental information that might serve to guide the development of new unsteady viscous theories and computational methods. A hierarchy of model problems can be developed, corresponding to increasing amounts of interaction between the viscous and inviscid parts of the flowfield. Within each level, specific sets of data are proposed that can be used as test cases for evaluating existing and future prediction methods.

The data for the present paper were obtained from the three airfoils shown in Fig. 1. Pressure and hot-wire instrumented models (0.62 m chord and 2.1 m span) were oscillated in pitch ($\alpha = \alpha_0 + \alpha_1 \sin\omega t$) about an axis at $x/c = 0.25$ in a 2.1×3.0 m atmospheric pressure, solid-wall wind tunnel. The effects of the tunnel walls are estimated to be small, but not negligible.

The freestream Mach number was varied between 0.07 and 0.30, with important consequences[1]; however, only the data at $M_\infty = 0.30$ are presented here. For this Mach number, the Reynolds number was approximately 4×10^6 based on chord, and the reduced frequency parameter, $k = \omega c/2U_\infty$, varied from 0 to 0.20.

Details of the instrumentation, experimental procedures, measurement uncertainties, and test conditions, as well as the coordinates of each airfoil, are documented in Ref. 2. That reference also describes the computer data tapes for the complete test program.

II. Summary of the Viscous-Inviscid Interaction Regimes

The overall features of the flowfield around an airfoil in subsonic flow are primarily characterized by the degree or extent of flow separation. For a given airfoil, the primary parameter that determines the degree of separation is the maximum angle of attack ($\alpha_{max} = \alpha_0 + \alpha_1$ for sinusoidal oscillations). An important aspect of the flows discussed in this paper is the large amplitudes α_1 that produce the large maximum angles. This contrasts with the hierarchy of viscous effects on oscillating airfoils at transonic speeds and low angles of attack, where the scale of the interaction is governed primarily by the strength and motion of the shock wave.[3,4] So far, prediction methods for this class of problems have not been successful for the low-speed, high-angle problems, and vice versa.

The importance of α_{max} is illustrated in Fig. 2, which portrays four important regimes of viscous-inviscid interaction for oscillating airfoils. For the left-hand part of the figure, that is, $\alpha_{max} = 13$ deg, there was almost no separation throughout the cycle and the viscous effects were small. When

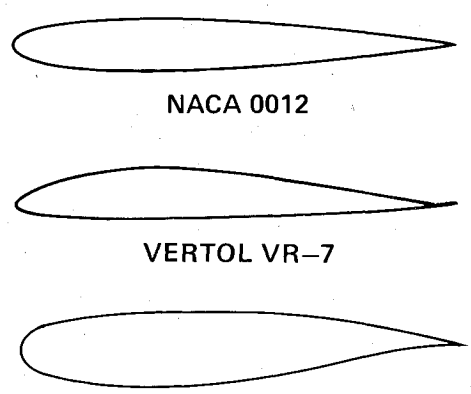

Fig. 1 Airfoil cross sections.

Presented as Paper 81-0051 at the AIAA 19th Aerospace Sciences Meeting, St. Louis, Mo., Jan. 12-15, 1981; submitted Feb. 20, 1981; revision received July 13, 1981. This paper is declared a work of the U.S. Government and therefore is in the public domain.

*Senior Staff Scientist, NASA Thermo- and Gas-Dynamics Division. Associate Fellow AIAA.
†Research Engineer. Member AIAA.

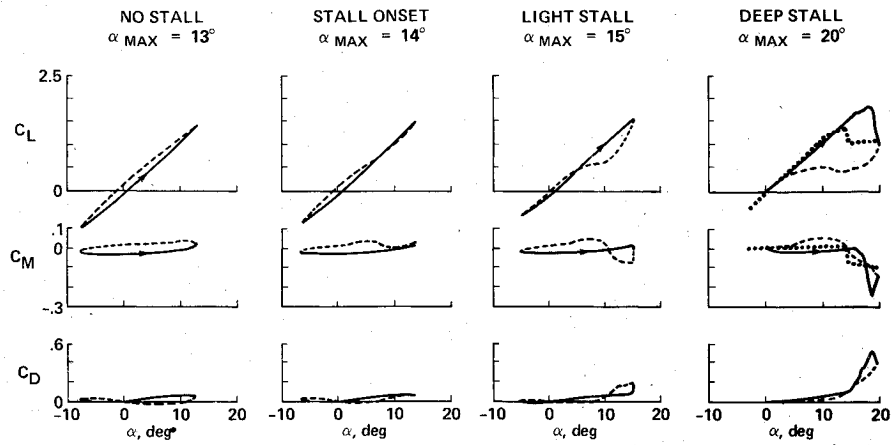

Fig. 2 Four regimes of unsteady airloads on the NACA 0012 airfoil; solid lines denote increasing angle of attack, dashed lines decreasing α, dotted lines static data.

α_{max} was increased to 14 deg, a limited amount of separation occurred during a small fraction of the cycle and distorted the hysteresis loops of the unsteady pressures and airloads. From a practical standpoint, the effect on C_M is particularly important. This stall-onset condition represents the limiting case of the maximum lift that can be obtained with no significant penalty in pitching moment or drag.

A slight additional increase in α_{max} to 15 deg produced a major increase in the extent, severity, and duration of the separation phenomenon for the conditions shown in Fig. 2. This type of viscous-inviscid interaction produced what is called light dynamic stall.[1] Further increases in α_{max} led to the deep dynamic stall regime, with a large viscous zone over the entire upper surface of the airfoil during a large fraction of the cycle.

Within each of the stall regimes shown in Fig. 2, the details of the flowfield depend on Mach number, Reynolds number, airfoil shape, and the airfoil motion $\alpha(t)$. To a first approximation, M_∞ and the leading-edge geometry are the principal determinants of the type of boundary-layer separation (for example, leading-edge, trailing-edge, or mixed separation characteristics), although changes from one type to another can occur as the frequency of the oscillation increases.[1] For a given class of separation or stall behavior, the amplitude α_1 and reduced frequency $k=\omega c/2U_\infty$ largely determine the stall and reattachment angles and the size and shape of the hysteresis loops, or, alternatively, the departure from quasistatic behavior.

More detailed descriptions of the various stall mechanisms can be found in Refs. 1, 5-7, and elsewhere. However, it is apparent from the brief remarks above that passing from no stall to deep dynamic stall encompasses a wide range of viscous flow phenomena, and that realistic but efficient prediction methods should probably be tailored to the specific characteristics of the flow regime of interest. The following sections provide some specific experimental information and test cases that can be used in developing and validating new analyses and computations for each regime depicted in Fig. 2. The test cases are arranged in the order of increasing levels of flow complexity and anticipated difficulty for theoretical predictions.

III. No Stall: Weak Interactions

If viscous effects are confined to thin boundary layers, the primary effects of oscillation can be derived from unsteady thin-airfoil theory. However, accurate quantitative predictions of secondary effects such as airfoil thickness and camber, finite mean angle of attack, large amplitude motion, boundary-layer displacement thickness, and wind tunnel wall corrections are not trivial. Consequently, experimental test cases in this weak interaction regime represent the first level in the hierarchy of model problems to be considered.

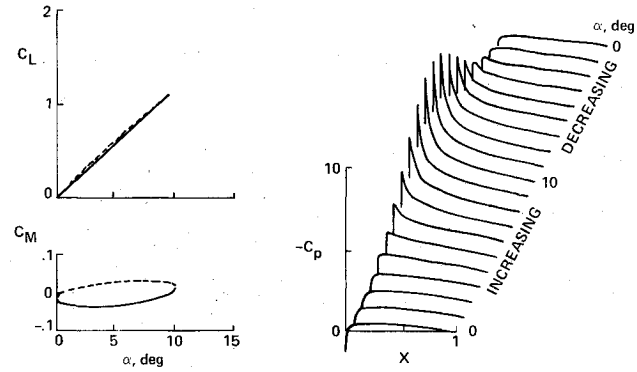

Fig. 3 Unsteady pressures and airloads for case 1, NACA 0012 airfoil, $\alpha=5°+5°\sin\omega t$.

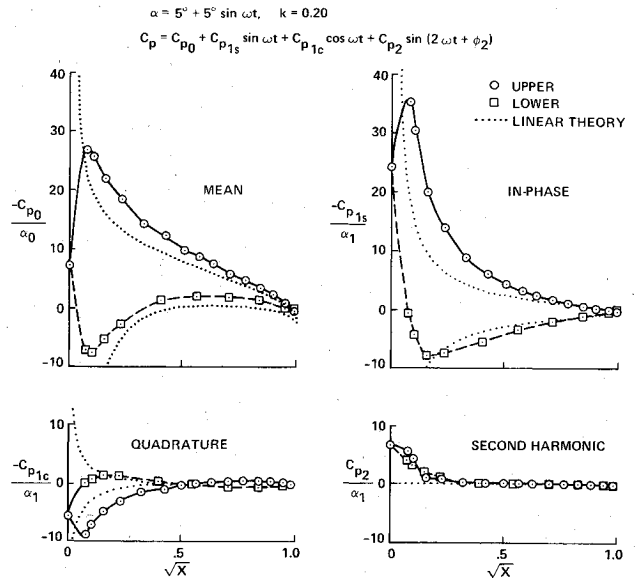

Fig. 4 Harmonic components of unsteady pressures for case 1, NACA 0012 airfoil, $\alpha=5°+5°\sin\omega t$.

Case 1: NACA 0012, $\alpha=5°+5°\sin\omega t$, $k=0.20$

Figure 3 illustrates the basic features of an oscillating airfoil with α_{max} rather large but well below the static stall angle. The boundary layers on both the upper and lower surfaces were fully attached throughout the cycle, except for a small separation bubble near the upper surface leading edge for $\alpha \gtrsim 5$ deg, which produced transition from laminar to turbulent flow.

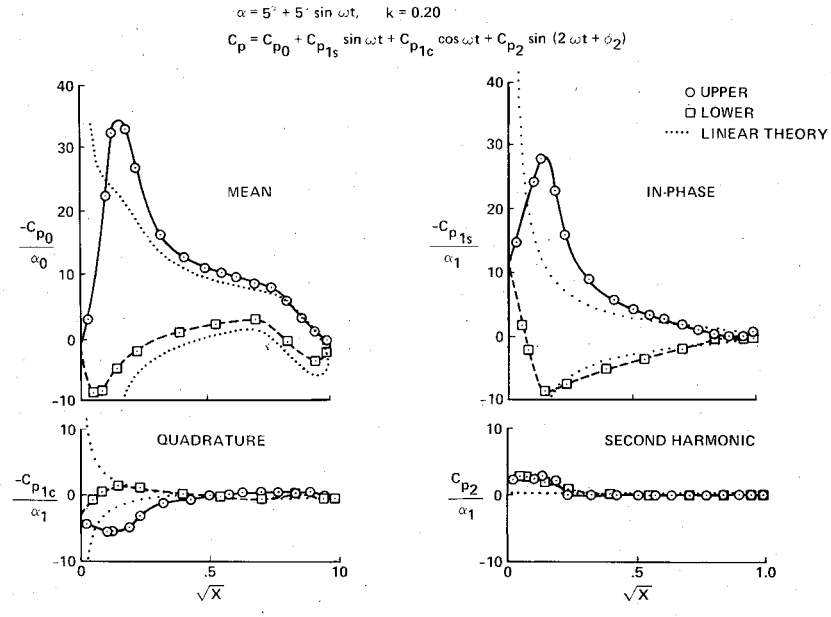

Fig. 5 Harmonic components of unsteady pressures for case 2, NLR-7301 airfoil, $\alpha = 5° + 5° \sin\omega t$.

Figure 4 shows the details of the unsteady pressure distributions by harmonic components. The C_p values are plotted vs $\sqrt{X}$ rather than X. This is done to stretch out the leading-edge region where the variations, and the discrepancies with linear theory, are the greatest. Linear theory predicts $C_{p2} = 0$ and equal and opposite values for the upper and lower surface components of C_{pI} given by the solution for an oscillating flat plate. The mean pressure C_{p0} is comprised of small-disturbance components due to thickness, camber, and mean angle. While this gives the right qualitative behavior, Fig. 4 shows that the predictions of linear theory are clearly not accurate for the present mean angle, amplitude, and airfoil geometry.

In Fig. 3, the hysteresis in C_L vs α is slightly different from that predicted by linear theory. This small difference, also evident in the results on the other profiles, might be ascribed to nonlinear effects of airfoil thickness, but it is also the trend predicted for wall interference effects.[8] In view of the uncertainty of applying standard wall correction to cases with large angles of attack and with possible separation, it is therefore recommended that computations or analyses of all of the cases in this paper include the solid wind tunnel walls as outer boundaries, rather than free air conditions.

Case 2: NLR-7301, $\alpha = 5° + 5° \sin\omega t$, $k = 0.20$

Differing from case 1 only in airfoil geometry, case 2 produced the data plotted in Fig. 5. Large effects of both thickness and camber are apparent in the mean pressure distribution, as would be expected. However, the fluctuating pressures appear to be much less sensitive to the large aft camber and are mainly affected by the blunt leading-edge geometry. The leading-edge radius is 3.5 times that of the 0012 airfoil and, consequently, the peak values of C_{pI} near the leading edge are less on the NLR-7301 airfoil. It should be noted that linear theory predicts the fluctuating pressures to be independent of airfoil geometry and mean angle and hence identical to those of case 1.

Case 3: NACA 0012, $\alpha = 8° + 5° \sin\omega t$, $k = 0.20$

Figure 6 shows the principal results of this more complex case. Increasing α_{max} has two main effects compared with case 1. First, the fluctuating pressures increase due to the nonlinear contributions of mean angle effects. Second, the upper surface boundary layer thickens, especially near the trailing edge. The former effect is most pronounced for the in-phase pressure distribution near the leading edge, whereas the latter is the main reason for the change in the out-of-phase

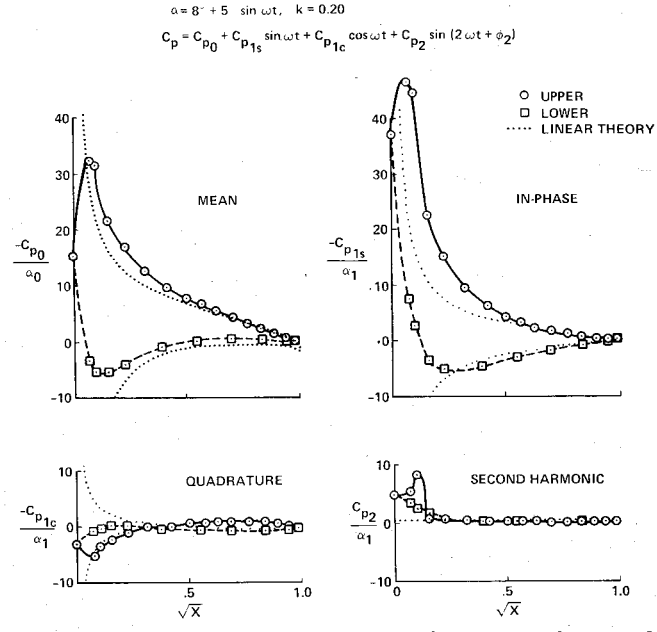

Fig. 6 Harmonic components of unsteady pressures for case 3, NACA 0012 airfoil, $\alpha = 8° + 5° \sin\omega t$.

component of C_p. This change in quadrature pressure is also reflected in the sense of the C_L-α hysteresis loop (not shown), which was opposite that of the two previous cases. Such behavior is not predicted by linear inviscid theory, but it presumably could be reproduced by including a coupled boundary-layer analysis.

Case 4: NLR-7301, $\alpha = 10° + 5° \sin\omega t$, $k = 0.20$

In case 4, a thin layer of reversed boundary-layer flow was detected moving forward from the trailing edge to approximately midchord as α approached α_{max}. The front edge of this reversed flow layer then retreated toward the trailing edge as α decreased to α_0 without ever producing large-scale separation of the boundary layer. However, the interaction with the inviscid flow produced the distortions in the fluctuating pressure distribution on the rear half of the airfoil that are evident in Fig. 7. The changes in C_{pI} between Figs. 5 and 7 are indicative of the effects of mild trailing-edge separation on this airfoil and on the VR-7 section.

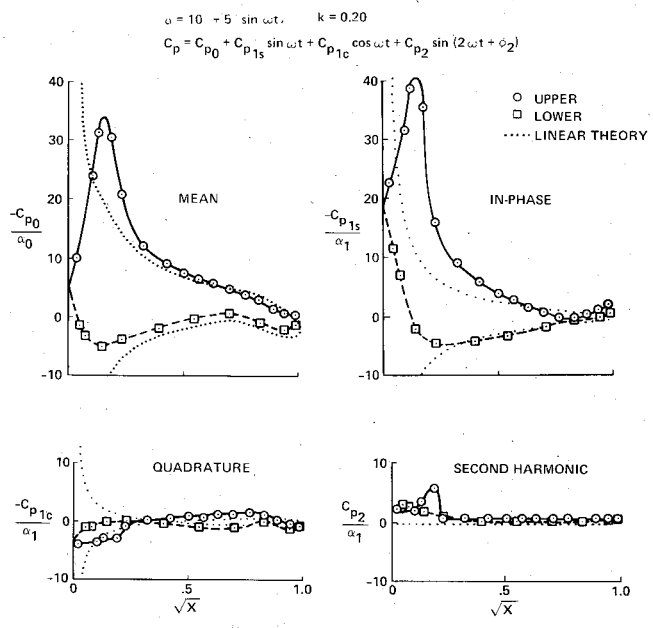

Fig. 7 Harmonic components of unsteady pressures for case 4, NLR-7301 airfoil, $\alpha = 10° + 5° \sin\omega t$.

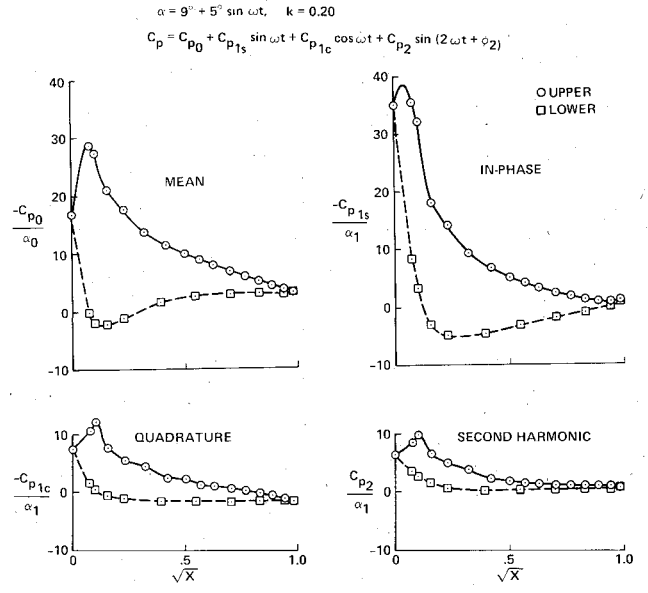

Fig. 9 Harmonic components of unsteady pressures for case 5, NACA 0012 airfoil, $\alpha = 9° + 5° \sin\omega t$.

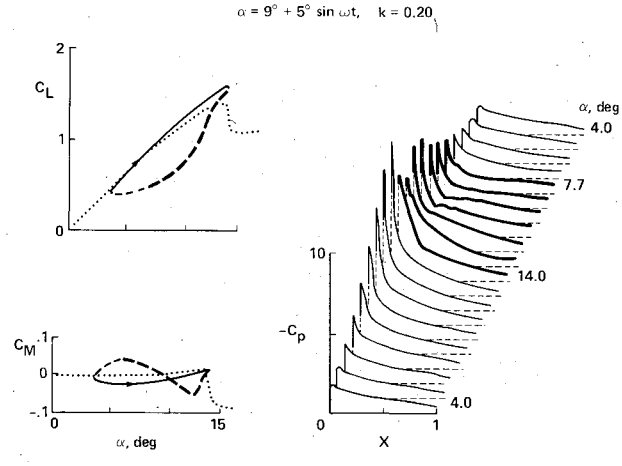

Fig. 8 Unsteady pressures and airloads for case 5, NACA 0012.

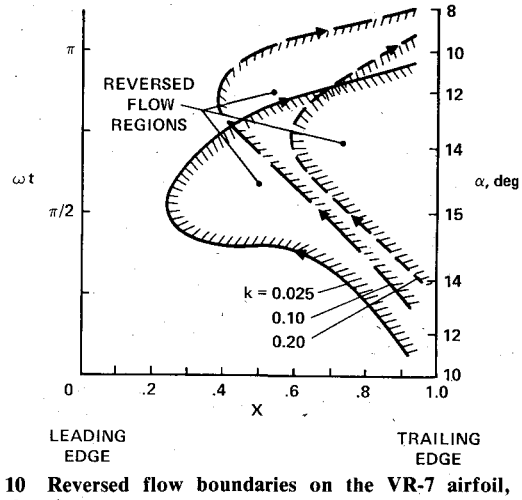

Fig. 10 Reversed flow boundaries on the VR-7 airfoil, case 6, $\alpha = 10° + 5° \sin\omega t$.

In both Figs. 6 and 7, unusual peaks appear in C_{p2} near the leading edge on the upper surface. These are due to small leading-edge separation bubbles that are not directly related to the boundary-layer behavior on the rear of the airfoils.

IV. Stall Onset: Mild Interaction

General Features

This regime has a special practical significance, as discussed in Sec. II. For the purposes of mathematical modeling, the no-stall and stall-onset regimes are similar, since the viscous layers remain relatively thin. However, the challenge to prediction methods is greater, because the magnitude of the viscous-inviscid interaction increases rapidly with small increases in α_{max} in the stall-onset regime. Furthermore, depending on the airfoil geometry and M_∞, the extent of flow separation may either increase or decrease with increasing reduced frequency, whereas viscous effects tend to be suppressed by unsteady effects below stall. As a result of these factors, the stall-onset regime is a narrow but important one that bridges the no-stall and light-stall domains.

Case 5: NACA 0012, $\alpha = 9° + 5° \sin\omega t$, $k = 0.20$

In the unsteady experiments at $M_\infty = 0.30$, a thin tongue of reversed flow akin to that of case 4 was observed on the rear of the NACA 0012 airfoil for 13 deg $\leq \alpha_{max} \leq$ 13.9 deg. For $k \leq 0.05$, this situation also existed for $\alpha_{max} = 14$ deg, but when the reduced frequency was increased above 0.10, unusual separation-like boundary-layer disturbances originated in the upper leading-edge region and propagated downstream. The boundary-layer instrumentation indicated neither reversed flow over the whole airfoil nor complete separation in the sense of a large-scale breakdown of the flow, but the thickening of the viscous layer was sufficient to cause significant distortions in the upper surface pressure distributions and in the hysteresis loops of C_L and C_M vs α. This is indicated by the bold curves in Fig. 8.

Figure 9 shows the harmonic components of the pressure distribution for this case. All four parts of the figure are different from those of the preceding no-stall case, $\alpha_{max} = 13$ deg, shown in Fig. 6. In particular, the large changes in the out-of-phase and second harmonic components over such a small increment in α_{max} indicate the onset of highly nonlinear behavior.

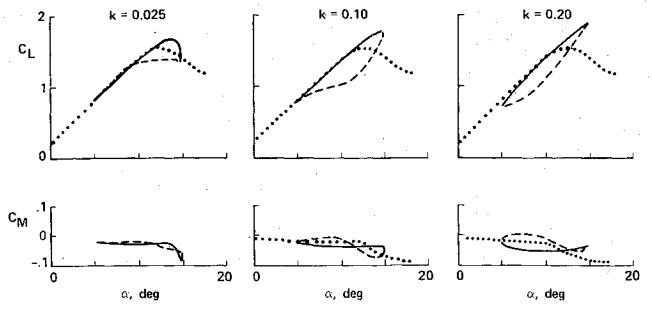

Fig. 11 Unsteady airloads for case 6, VR-7 airfoil, $\alpha = 10° + 5° \sin\omega t$.

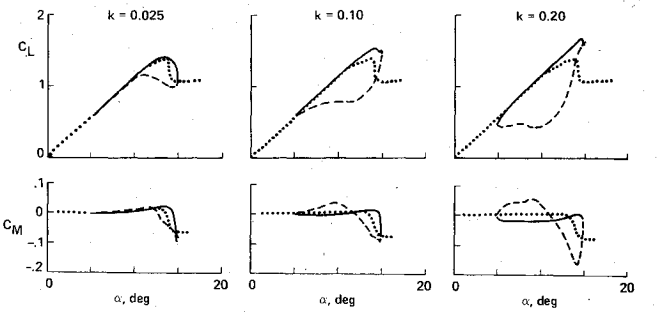

Fig. 12 Unsteady airloads for case 7, NACA 0012 airfoil, $\alpha = 10° + 5° \sin\omega t$.

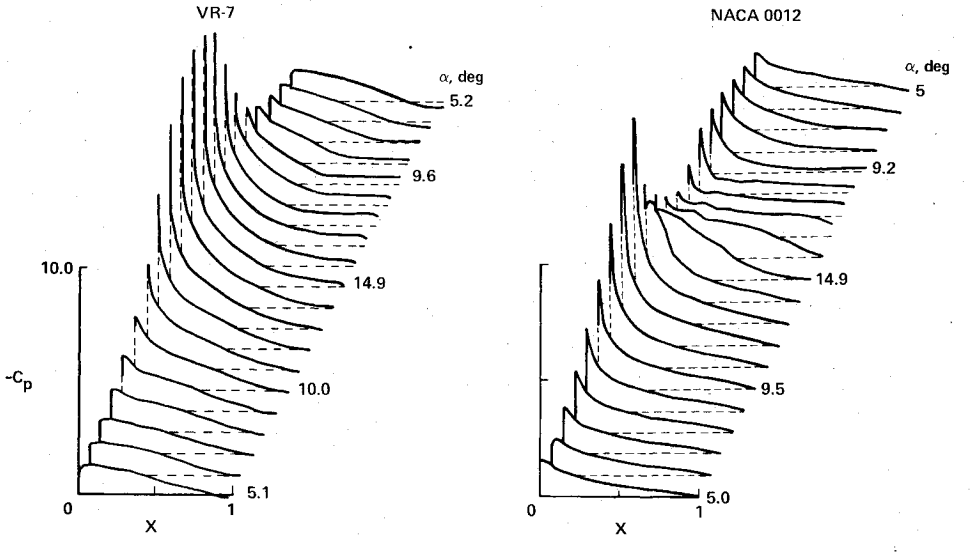

Fig. 13 Unsteady pressures for cases 6 and 7, $\alpha = 10° + 5° \sin\omega t$, $k = 0.20$.

Case 6: Vertol VR-7, $\alpha = 10° + 5° \sin\omega t$, $0.01 \le k \le 0.20$

In contrast to the NACA 0012 section, a well-defined thin layer of reversed viscous flow developed in the trailing-edge region in the stall-onset and light-stall regimes with the VR-7 airfoil. For case 6, the chordwise extent of this reversed flow was strongly dependent on reduced frequency. This is illustrated in Fig. 10, which shows the loci of the point $\tau_w \cong 0$ on the airfoil surface as a function of time for three values of k. The reversed-flow region is clearly delayed and suppressed by increasing unsteady effects.

In a qualitative sense, the upper surface pressure distributions were not significantly distorted by the viscous effects over the experimental range of frequencies. However, Fig. 11 shows that the extent of the trailing-edge separation has an important quantitative effect, and only the example at $k = 0.20$ can be considered truly representative of stall onset. For $k \le 0.10$, the results exhibit many of the characteristics of the next level in the hierarchy, light stall.

V. Light Stall: Strong Interaction

General Features

This regime for oscillating airfoils shares some of the general features of classical static stall, such as a loss of lift and significant increases in drag and nose-down pitching moment compared with the theoretical inviscid values, when α exceeds a certain value. However, the unsteady stall behavior is characterized by large phase lags and hystereses in the separation and reattachment of the viscous flow and, consequently, in the airloads. Also, the aerodynamic damping in pitch, given by $\oint C_M d\alpha$, can become negative, and this unstable tendency is strongest in the light-stall domain.

Another distinguishing feature of this regime is the scale of the interaction. The vertical extent of the viscous zone tends to remain on the order of the airfoil thickness, generally less than for static stall. Consequently, this class of oscillating airfoil problems should be within the scope of zonal methods or thin-layer Navier-Stokes calculations, with relatively straightforward turbulence modeling.

The qualitative behavior of light stall is known to be especially sensitive to airfoil geometry, reduced frequency, maximum incidence, and Mach number; also, three-dimensional effects and the type of motion are probably important. The quantitative behavior is closely related to the boundary-layer separation characteristics (for example, leading-edge vs trailing-edge separation) and to the changes in this separation behavior with α_{max}, k, and M_∞. Therefore, the possible test cases are numerous and varied. For the sake of simplicity, however, this section will concentrate on the effects of reduced frequency on two airfoils: one with trailing-edge separation characteristics and one with leading-edge separation behavior. An important test of prediction techniques would be to distinguish between these two types of separation and to predict correctly the very different trends that each engenders as reduced frequency increases.

Trailing-edge separation is represented by case 6, discussed earlier and presented in Figs. 10 and 11. The important point here is the suppression of the amount of trailing-edge separation, and hence the magnitude of the viscous-inviscid interaction, with increasing frequency. As a result of this unsteady effect, case 6 passes from light-stall behavior for $k \le 0.10$ to stall-onset conditions for $k \ge 0.15$.

Case 7: NACA 0012, $\alpha = 10° + 5° \sin\omega t$, $0.01 \le k \le 0.20$

For $M_\infty \le 0.2$, the light-stall behavior of the 0012 airfoil followed the trends of case 6; that is, separation was sup-

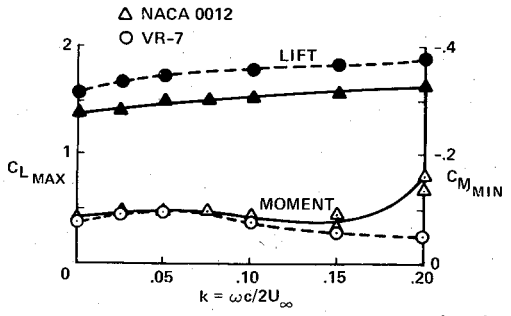

Fig. 14 Maximum lift and moment values for $\alpha = 10° + 5° \sin\omega t$.

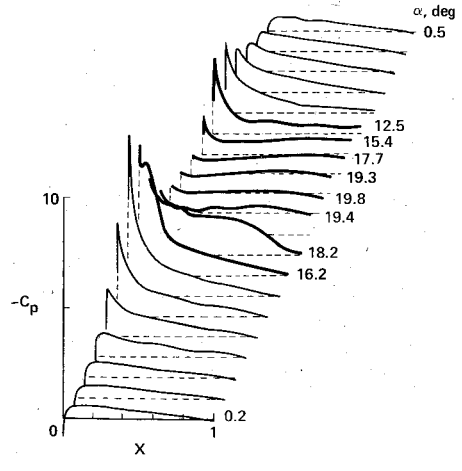

Fig. 15 Unsteady pressures for case 8, NACA 0012 airfoil, $\alpha = 10° + 10° \sin\omega t$, $k = 0.10$.

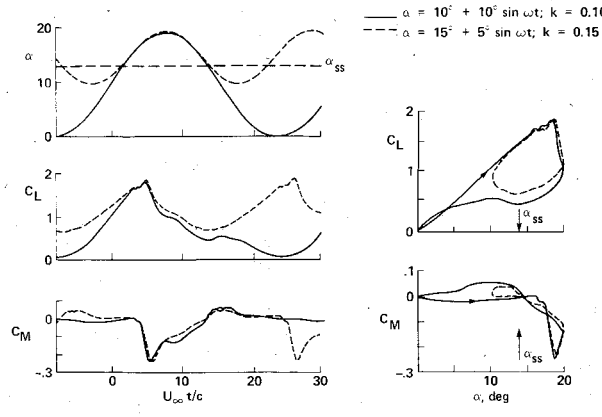

Fig. 16 Unsteady airloads on the NACA 0012 airfoil, cases 8 and 9.

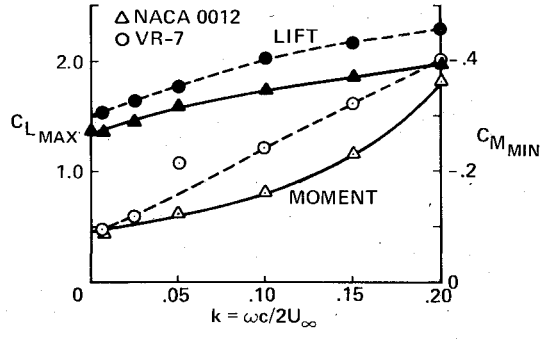

Fig. 17 Maximum lift and moment values for $\alpha = 15° + 5° \sin\omega t$.

pressed as k increased. However, at $M_\infty = 0.30$ the severity of the stall increased with increasing k, as the mild trailing-edge separation at low frequency gave way to the separation-like leading-edge disturbances that were noted for case 5 for $k \geq 0.15$.

The attendant changes in the lift and pitching moment behavior are shown in Fig. 12, which provides a striking contrast to the VR-7 data in Fig. 11. The upper surface pressure distributions for the two airfoils are shown in Fig. 13 for $k = 0.20$, where the differences are the most pronounced. Particularly noteworthy is the collapse of the leading-edge suction on the NACA 0012 airfoil when stall occurs. This seems to be a general characteristic of leading-edge stall, in contrast to the VR-7 profile with trailing-edge stall.

The maximum lift rose monotonically with k for both the 0012 and VR-7 airfoils, as shown in Fig. 14. However, the figure shows that the trends of $C_{M_{min}}$ are quite different for $k > 0.10$, as the stall became more severe for the 0012 section. In fact, the behavior of C_M vs α at $k = 0.20$ and the collapse of the leading-edge suction (Fig. 13b) are characteristics that become even more accentuated in deep dynamic stall, which is the next level in the hierarchy.

VI. Deep Dynamic Stall: Viscous Dominated

General Features

The time-dependent stall behavior in this regime is characterized by the shedding of a large vortex-like disturbance from the leading-edge region and the passage of this vortex over the upper surface of the airfoil.[1,5-7] This produces values of C_L, C_M, and C_D that are far in excess of their static counterparts when α is increasing, and large amounts of hysteresis occur during the rest of the cycle. The scale of the interaction zone is also large; the thickness of the viscous layer is of the order of the airfoil chord during the vortex-shedding process. This poses potential problems in grid generation, spatial resolution, and turbulence modeling for numerical analyses.

This qualitative picture appears to hold over a wide range of unsteady flow conditions, airfoil geometries, Reynolds numbers, and Mach numbers, provided strong shock waves do not develop.[1,7] The quantitative behavior of the flow depends primarily on the time history of the angle of attack for the portion of the cycle when α exceeds the static stall angle α_{ss}. This feature and other details of the flow behavior will become evident in the following examples.

Case 8: NACA 0012, $\alpha = 10° + 10° \sin\omega t$, $k = 0.10$

The right-hand section in Fig. 2 shows one of the examples of deep dynamic stall for the NACA 0012 airfoil. The contrast with the static behavior and with the other unsteady stall regimes is readily apparent.

Figure 15 shows the unsteady pressure distribution on the upper surface for this case. In particular, the vortex-shedding phenomenon manifests itself in the curves at $\alpha = 16.2$, 18.2, and 19.4 deg, and the leading-edge suction collapses abruptly over this interval. The boundary layer separated initially from the leading-edge region at this frequency, starting at $\alpha \cong 16$ deg, or $\omega t \cong 40$ deg. This represented a change from abrupt trailing-edge stall[1] at $k \leq 0.05$.

Case 9: NACA 0012, $\alpha = 15° + 5° \sin\omega t$, $0.01 \leq k \leq 0.20$

One particular reduced frequency of this set of data, $k = 0.15$, produced results almost identical to those of case 8 over the portion of the cycle for which $\alpha \geq \alpha_{ss}$. Figure 16 shows the time histories of α, C_L, and C_M and the corresponding hysteresis loops of C_L and C_M vs α superimposed on those of case 8. The agreement between these cases is remarkable; but it should be emphasized that the

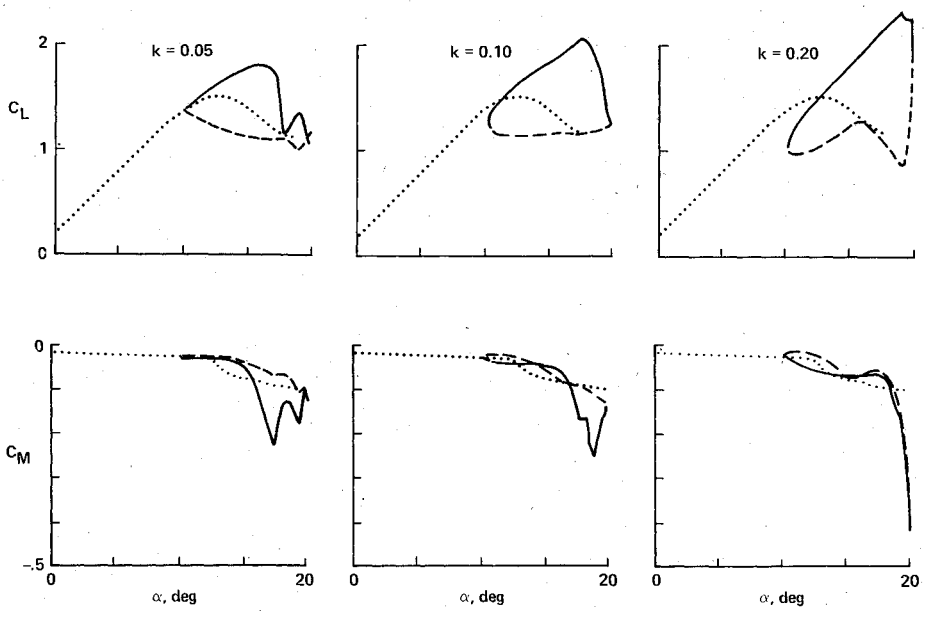

Fig. 18 Unsteady airloads for case 10, VR-7 airfoil, $\alpha = 15° + 5° \sin\omega t$.

results match this well only when the time histories of α agree.[1]

Figure 17 shows the growth of $C_{L_{max}}$ and $C_{M_{min}}$ with reduced frequency for the NACA 0012, along with the Vertol VR-7 results of the following case. The extreme values of $C_{M_{min}}$ are particularly noteworthy, as they are considerably larger than the light-stall results shown in Fig. 14.

Case 10: Vertol VR-7, $\alpha = 15° + 5° \sin\omega t$, $0.01 \leq k \leq 0.20$

At lower Mach numbers, the VR-7 airfoil exhibited trailing-edge separation behavior throughout the light- and deep-stall regimes. However, at $M_\infty = 0.30$ an interesting change occurred in the boundary-layer characteristics, from trailing-edge separation to a mixed leading- and trailing-edge stall, as the vortex shedding phenomenon increased in intensity with increasing k. This produced the lift and moment behavior shown in Fig. 18, which varied differently with k than the light-stall results shown earlier in Fig. 11.

The effects of vortex shedding first appeared at $k \cong 0.05$, with a weak vortex originating around midchord. The flow reversal that preceded this vortex formation progressed slowly upstream from the trailing edge. However, a conversion to leading-edge stall began for $k \geq 0.15$ with a much stronger vortex originating at $x \cong 0.02$. It is the distortions in the chordwise pressure distribution due to this transient vortex that produce the large values of the pitching moment that are indicated in Figs. 17 and 18. A more complete discussion of this particular case, including boundary-layer flow reversal data and unsteady pressure distributions, is given in Ref. 1.

VII. Concluding Remarks

The 10 cases described in the previous sections illustrate most, although by no means all, of the panorama of viscous-inviscid interactions that occur on oscillating airfoils in subsonic flow. The specific flow conditions for each case were carefully selected to emphasize the predominant characteristics of each of the four flow regimes, while minimizing the effect of the experimental uncertainties in the appropriate data. In other words, the experimental results were presented more on the basis of documenting specific trends or features of each flow, rather than on the importance of the absolute values of the measurements. Nevertheless, the data are thought to be of sufficiently high quality that including the effects of the wind-tunnel walls would be warranted in any analysis of the test cases.

To the authors' knowledge, few of the specific cases, or their equivalents, discussed in this paper have yet been calculated. However, the unstalled cases of Sec. III would appear to be well suited to straightforward extensions of present-day zonal modeling methods for steady flows, as exemplified by the recent collection of papers in Ref. 9. Such methods should also be capable of treating the stall-onset cases of Sec. IV, although the details of the unsteady flow regions with flow reversal at the bottom of the boundary layer will surely require special treatment. The thin-layer, Reynolds-averaged Navier-Stokes methods (e.g., Ref. 10) are also appropriate for this regime, as well as for the light-stall regime. The extent to which the zonal methods can be applied to the light-stall cases is an open question. However, both approaches offer attractive alternatives to the empirical correlation methods that are currently used for engineering predictions.[6,7] For this reason, coupled with its practical importance, the light-stall regime is probably the one that most warrants concentrated research efforts.

On the other hand, the greatest challenge to theoretical or numerical analysis is clearly the deep-stall regime. As mentioned in Sec. VI, the viscous region is very large, and it is a dominant feature of the flowfield, so that thin-layer approximations and turbulence models based on boundary-layer length scales are probably suspect. New approximate or semiempirical methods that take advantage of the predominance of the vortex-shedding phenomena might be feasible, in addition to the discrete-vortex methods[6,7] that are sometimes applied to bluff-body flows, provided they are not limited by the assumptions that have to be made to start the calculations. The long-range need seems to be for Navier-Stokes calculations with improved turbulence modeling. In any case, a viable method should reproduce the universal vortex-shedding phenomenon *and* the quantitative differences in the three cases presented.

In conclusion, the experimental results described in this paper provide well-defined conditions and data that can be used to evaluate existing theoretical and numerical prediction methods. The information presented should also help future investigators decide on the approach that is the most appropriate for the particular domains of interest to them.

Acknowledgment

Calculations of the unsteady linear pressure distributions in Fig. 4 were kindly supplied by Dr. S. R. Bland of the NASA Langley Research Center.

References

[1] McCroskey, W. J., McAlister, K. W., Carr, L. W., Pucci, S. L., Lambert, O., and Indergand, R. F., "Dynamic Stall on Advanced Airfoil Sections," *Journal of the American Helicopter Society*, Vol. 26, No. 3, July 1981, pp. 40-50.

[2] McCroskey, W. J., McAlister, K. W., Pucci, S. L., Carr, L. W., Lambert, O., and Indergand, R. F., "An Experimental Study of Dynamic Stall on Advanced Airfoil Sections," NASA TM in press.

[3] Davis, S. S. and Malcolm, G. N., "Unsteady Aerodynamics of Conventional and Supercritical Airfoils," AIAA Paper 80-0734, April 1980.

[4] Dowell, E. H., Bland, S. R., and Williams, M. H., "Linear/Nonlinear Behavior in Unsteady Transonic Aerodynamics," AIAA Paper 81-0643, April 1981.

[5] Young, W. H. Jr., "Fluid Mechanics Mechanisms in the Stall Process of Airfoils for Helicopters," Paper presented at Symposium on Numerical and Physical Aspects of Aerodynamic Flows, Long Beach, Calif., Jan. 1981.

[6] Beddoes, T. S., "A Qualitative Discussion of Dynamic Stall," and "Prediction Methods for Unsteady Separated Flows," Papers 3 and 15, *Special Course on Unsteady Aerodynamics*, AGARD Rept. R-679, June 1980.

[7] McCroskey, W. J., "The Phenomenon of Dynamic Stall," NASA TM-81264, March 1981.

[8] Fromme, J. A., Golberg, M. A., and Werth, J., "Unsteady Two-Dimensional Airloads Acting on Oscillating Thin Airfoils in Subsonic Ventilated Wind Tunnels," NASA CR-2967, 1978.

[9] Monnerie, B. and Quinn, B., eds., "Computation of Viscous-Inviscid Interactions," AGARD Conference Proceedings CP-291, Oct. 1980.

[10] Baldwin, B. S. and Lomax, H., "Thin Layer Approximation and Algebraic Model for Separated Turbulent Flows," AIAA Paper 78-257, Jan. 1978.